

Multifractality in Surface Potential for Cancer Diagnosis

Phat K. Huynh¹, Dang Nguyen², Grace Binder³, Sharad Ambardar², Trung Q. Le^{1,2}, and
Dmitri V. Voronine^{2,4*}

¹ Department of Industrial and Management Systems Engineering, University of South Florida,
Tampa, FL, 33620

² Department of Medical Engineering, University of South Florida, Tampa, FL, 33620

³ Department of Chemistry, University of South Florida, Tampa, FL, 33620

⁴ Department of Physics, University of South Florida, Tampa, FL, 33620

* Corresponding author: dmitri.voronine@gmail.com

Abstract

Recent advances in high-resolution biomedical imaging focusing on morphological, electrical, and biochemical properties of cells and tissues, scaling from cell clusters down to the molecular level, have improved cancer diagnosis. Multiscale imaging revealed high complexity that requires advanced data processing methods of multifractal analysis. We performed label-free multiscale imaging of surface potential variations in human ovarian and breast cancer cells using Kelvin probe force microscopy (KPFM). An improvement in the differentiation between normal and cancerous cells of for multifractal analysis using adaptive versus median threshold for image binarization was demonstrated. The results reveal the potential of using multifractality as a new biomarker for cancer diagnosis. Furthermore, the surface potential imaging can be used in combination with morphological imaging for cancer diagnosis.

Keywords: AFM, KPFM, breast cancer, ovarian cancer, fractal analysis, multifractal analysis

1. INTRODUCTION

Breast and ovarian are the most frequent types of cancer among women worldwide [1, 2]. Morbidity and mortality of cancer are substantially decreased with early detection [3]. Cytological screening tests have decreased mortality. However, these methods have insufficient sensitivity and are time-consuming in both analysis and training of professionals with subjective manual diagnosis. More accurate tests may substantially decrease the cost and patient inconvenience. Tumorigenesis is a complex process with an uncontrolled growth of cells that ignore apoptotic signals triggered by cell cycle dysregulation and modulate cell survival pathway signaling. This process involves remodeling of the extracellular matrix, accompanied by morphological and electrochemical changes in the plasma membrane. Nanoscale imaging techniques investigate these changes with a high spatial resolution to better understand tumorigenic mechanisms.

The plasma membrane resting potential was shown to undergo abnormal depolarization in cancer cells [4, 5]. Various mechanisms of membrane potential regulation have been investigated that involve cell signaling pathways mediated by the disrupted activities of ion channels, pumps, and transporters. The potential difference between tumor and paratumor was found for several types of cancer, and the resulting depolarization was correlated with metastasis [6]. The membrane potential has been identified as an important bioelectric marker that reflects the changes in cellular activities.

The common methods of membrane potential measurements based on electrodes and voltage-sensitive dyes have a lack of imaging and a limited spatial resolution, respectively. KPFM is a nanoscale electrostatic force imaging technique based on the contact potential difference (CPD) between a scanning probe tip and sample [7], which has been less commonly used for cell imaging. KPFM has a high spatial resolution of less than 10 nm, which is determined by the size of the tip apex. It was previously used in a variety of biomedical applications such as mapping the surface potential of biomolecules [8-10], including DNA [11, 12] proteins [13, 14], and plasma membrane of cells [15, 16], revealing biomolecular interactions at the single-molecule level [8, 17-19].

Nanoscale morphological measurements by atomic force microscopy (AFM) have previously been used for cancer detection [19-21]. AFM provides direct imaging of cell surface morphology with nanoscale resolution. Physical properties such as cell stiffness, adhesion, and elasticity were used to identify cancerous tissue [22, 23]. However, in some cases AFM morphological imaging cannot differentiate between normal and cancer cells, while adhesion maps showed differences in

fractality [24]. Fractal [25-30] and multifractal [31, 32] analyses were previously used for cancer diagnosis. Fractal geometry was used to describe the morphology of cancer cells and tissues by a single parameter, the fractal dimension, as a diagnostic biomarker [33, 34]. The change in fractal dimension or self-similar organization of surface morphology by malignant transformation can be quantified. Fractal dimension is suitable for the characterization of monofractal objects that have the same scaling exponent at different scales. However, a more complex organization (*e.g.*, cellular membrane) exhibits different fractal exponents at different scaling ranges resulting in several interwoven fractal sets, which are better described by the multifractal formalism [35, 36]. Fractal and multifractal analyses significantly improved the diagnostic efficiency of AFM imaging for cancer detection. However, the interpretation of complex morphologies was limited due to the lack of corresponding molecular information. KPFM is a nanoscale imaging technique based on molecular bioelectricity that can provide deeper insights.

In this work, we performed the fractal and multifractal analysis of morphological (AFM) and bioelectric (KPFM) images of ovarian and breast cells. The high spatial resolution allows for probing a broad range of scales, covering more than three orders of magnitude, from < 10 nm to tens of micrometers. We used the box-counting method to determine the fractal dimensions with significant variations at different scaling ranges. We used multifractal analysis for a more precise characterization of the scaling behavior, which showed a significant difference between the surface potential of the normal and cancer cells. We showed an improved efficiency of KPFM compared to AFM multifractality for cancer detection.

2. MATERIALS AND METHODS

2.1. Sample preparation

SHT290 and ES-2 cell lines

The human ovarian cancer ES-2 CCOC cell line (American Type Culture Collection, USA) [37] was cultured in MCDB 131: Media 199 (1:1 ratio) and McCoy's medium, respectively, supplemented with 10% FBS, 100 units/ml of penicillin and 100 μ g/ml of streptomycin. The immortalized normal human endometrial stromal cell line, SHT290 (Kerafast, USA) [38] was maintained in F12K : Media 199 (1:1 ratio) and supplemented with 5% FBS, 0.1% Mito, 2 μ g/ml of human insulin, 100 units/ml of penicillin and 100 μ g/ml of streptomycin. All cell cultures were

passed less than 10 times. Cell cultures were maintained in an incubator at 37°C and 5% CO₂ atmosphere.

MCF-10A and MDA-MB-231 cell lines

MCF-10A cells (Michigan Cancer Foundation) are a non-tumorigenic, immortalized mammary epithelial cell line, while MDA-MB-231 cells are triple-negative metastatic breast cancer epithelial cells [39-43] and were grown according to ATCC guidelines.

Fixation

All cells were cultured on atomically flat gold substrates (Tedpella) as required for KPFM measurements. Cells were washed with phosphate-buffered saline (PBS) before and after fixation to remove residual media or fixative solution, respectively. Samples were fixed using 4% paraformaldehyde (PFA) for 15 min at room temperature. After washing, fixed cells were stored in PBS with 0.01% sodium azide. Samples were rinsed with methanol prior to analysis.

AFM and KPFM

Both AFM and KPFM measurements were performed in tapping mode with an average tip-sample distance of 20 nm. AFM measurements were performed using Si tip, whereas KPFM measurements were performed using a conductive Au-coated Si tip. All images used for fractal and multifractal analysis were acquired with 3×3 μm² scan sizes, 512×512 data point resolution, and with a pixel size of ~ 6 nm. AFM and KPFM imaging were performed in air at ambient temperature (see schematic diagrams in supplementary Fig. S1).

2.2. Image sampling and image binarization using adaptive and median thresholding

Figure 1 shows the typical examples of the optical (Figs. 1a – 1d), AFM (Figs. 1e – 1h) and KPFM (Figs. 1i – 1l) images of the 37four cell lines used in this work. The cancer detection procedure involved the following steps. In step 1, the simultaneous AFM/KPFM image sampling was performed by scanning 3×3 μm areas selected on the cytoplasmic and nucleus parts of the cells with 512×512 pixel density as described in the Methods section (Fig. 1m). After normalization, in step 2, the image binarization was performed using either the adaptive threshold or median methods (Fig. 1n). In step 3, either the fractal or multifractal analysis was performed (Fig. 1o) that delivered parameters for the statistical analysis.

To convert 2D gray-scale AFM/KPFM images to binary images, we used two image binarization methods: adaptive and median thresholding. The adaptive image thresholding technique is called Bradley’s method [44], in which the method binarizes the gray-scale image using a locally adaptive threshold. The threshold was estimated for each pixel utilizing the local mean intensity around the neighborhood of the pixel. The adaptive method uses a neighborhood size of $\sim 1/8^{\text{th}}$ of the image size (64 pixels). If the current pixel value is less than the computed threshold, then it is set to black (i.e., value 0), otherwise, it is set to white (i.e., value 1). The median thresholding image binarization uses the median value of all pixels as a hard threshold and set the pixels whose values are larger than the median to black and set them to white otherwise.

2.3. Fractal and multifractal methods

Fractal analysis

Fractal dimension is a measure of the space-filling capacity of a fractal object relative to its embedding space [45]. Generally, the relationship between the number of coverings (e. g. boxes in the box-counting method) $N(a)$ and the scaling factor a (e. g. box length) is expressed as

$$N(a) \propto a^{-D} \tag{1}$$

where D is the fractal dimension that can take positive non-integer values. Equation (1) represents the scaling law, which describes self-similarity of a fractal object using a single parameter. The fractal dimension D was estimated by the box-counting method [46] using the fractal analysis MATLAB toolbox [47] by counting the number of boxes $N(a)$ with different side length a as

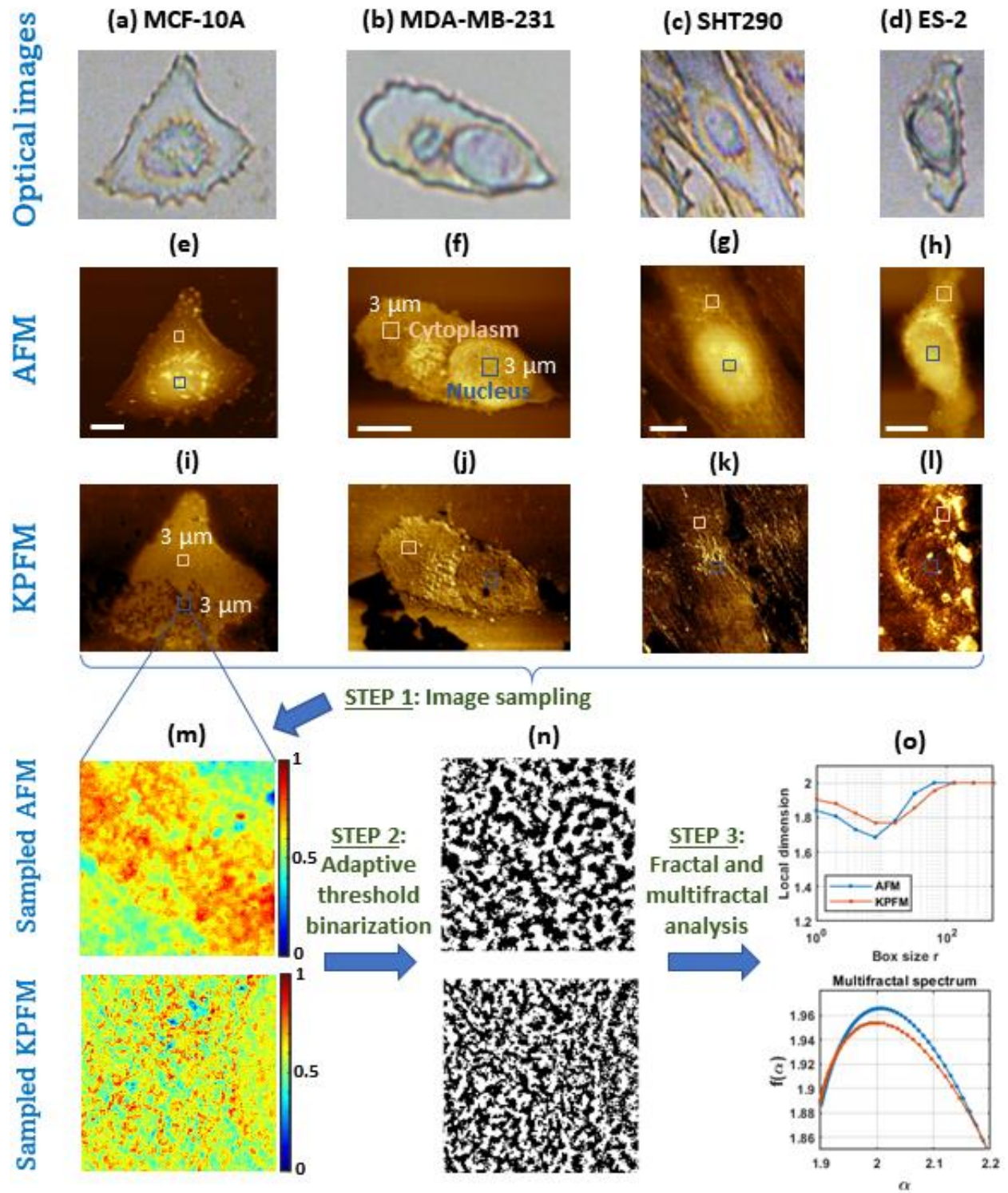


Figure 1. Illustration of the fractal and multifractal analysis procedure applied to AFM and KPFM images of normal (MCF-10a, SHT290) and cancer (MDA-MB-231, ES-2) cells. Scale bar in I – (h) is 10 μm.

$$D = \lim_{a \rightarrow 0} \frac{\ln N(a)}{\ln\left(\frac{1}{a}\right)}. \quad (2)$$

However, a single parameter describing the monofractal geometry is limited in the ability to completely differentiate the complex scaling behaviors of many real-life objects [48-51]. This is attributed to the fact that the fractal dimension D only characterizes the average fractality of multifractal objects via a simple scaling law [45, 52].

Multifractal analysis

Multifractal analysis addresses the limitations of the fractal analysis by providing a local description of the complex scaling behavior of biomedical images, represented as a spectrum of singularity exponents $f(\alpha)$ [31]. In the case of the binarized AFM/KPFM images, the local mass density $P_i(a)$ of the box centered at image location x_i with side length a is

$$P_i(a) = \frac{N_i(a)}{N}, \quad (3)$$

where $N_i(a)$ and N are the number of black pixels in box i of size a and the total number of pixels in box i , respectively. The scaling of $P_i(a)$ follows the power law, $P_i(a) = a^{\alpha_i}$, where $\alpha_i \equiv \alpha(x_i)$ is the singularity exponent describing the local scaling (local fractal behavior) centered at location x_i of the i^{th} box, which can be estimated as

$$\alpha_i = \lim_{a \rightarrow 0^+} \frac{\ln P_i(a)}{\ln(a)}. \quad (4)$$

The multifractal spectrum $f(\alpha)$ is defined as the fractal dimension of the set of locations x such that $\alpha(x) = \alpha$. The $f(\alpha)$ spectrum represents a statistical distribution of the singularity exponents α_i which characterizes the local singularity strength or multifractality of the image. It is practically estimated using the Legendre transformation as

$$f(\alpha) = q\alpha - \tau(q), \quad \alpha(q) = \frac{d\tau(q)}{dq}, \quad (5)$$

where q is the moment and $\tau(q)$ is the mass or Holder exponent [53]. In the multifractal formalism, $D_q = \tau(q)/(q - 1)$ is the generalized fractal dimension, for which D_0 ($q = 0$) is equivalent to the box-counting fractal dimension. Furthermore, the information dimension D_1 ($q = 1$) describes the

change of information entropy with the box size [54], whereas the correlation dimension D_2 ($q = 2$) quantifies the correlation of fractal measures in the boxes [55]. In addition, the width of the singularity spectrum $\Delta\alpha(Q) = \alpha_{max}(Q) - \alpha_{min}(Q)$, where $\alpha_{max} = \max\{\alpha(q), q \in [-Q, Q]\}$ and $\alpha_{min} = \min\{\alpha(q), q \in [-Q, Q]\}$, is the measure of multifractality [43]. The variation of the generalized fractal dimension D_q over a range of q , known as the Rényi spectrum, characterizes the multifractal behavior of images, with the broader range of the sigmoidal curve corresponding to the more heterogeneous scaling [43, 56, 57]. The multifractal analysis was performed using the a MATLAB toolbox [49].

2.4. Statistical analysis and hypothesis testing

To determine if the differences of the estimated multifractal parameters (D_0 , D_1 , D_2 , and $\Delta\alpha(4)$) between the MCF-10A (normal) vs MDA-MB-231 (cancer) cell lines and SHT290 (normal) vs ES-2 (cancer) cell lines are statistically significant, two-sample t -test was performed on the measurements of the multifractal parameters, which were obtained from both AFM and KPFM images. The null hypothesis states that the random samples are from normal distributions with equal means and equal but unknown variances, and the alternative hypothesis states that the samples come from populations with unequal means. We used $n_1 = 4$ and $n_2 = 8$ number of AFM images for MCF-10A vs MDA-MB-231, and $n_1 = 5$ and $n_2 = 3$ for SHT290 vs ES-2 cells. We used $n_1 = 2$ and $n_2 = 11$ number of KPFM images for MCF-10A vs MDA-MB-231, and $n_1 = 3$ and $n_2 = 5$ for SHT290 vs ES-2 cells.

3. RESULTS

Typical representative examples of the AFM and KPFM images of the four cell lines and their corresponding binarized images, local fractal dimensions, and multifractal spectra using the adaptive and median value thresholding methods are shown in supplementary Figs. S2 and S3 (see Supplementary Information). The thresholding values of the image binarization cut-off were estimated based on the median value of all pixels for the median method and the local mean intensity of the pixel neighborhood for the adaptive method, as described in the Methods section. The adaptive method results were more consistent and showed better statistical significance in distinguishing normal and cancer cells as described below. This may be due to the presence of the

occasional random dust particles on the sample that have a large height in AFM images, affecting the median height values. This effect is minimized in the adaptive method. Therefore, we selected the adaptive method below to demonstrate the results. We included the median method results in the supplementary Figs. S2 and S3 for comparison. While both methods showed similar results for most of the cells, some of the data showed significant differences due to the random fluctuations, which were especially pronounced in the AFM height images. For example, Figs. S2m and S2q show similar fractal and multifractal AFM plots for an MCF-10A cell, while Figs. S2n and S2r show large differences for an MDA-MB-231 cell. However, the corresponding KPFM signals from the same cells showed similar plots in Figs. S2o, S2p, S2s and S2t. Similar trends are observed for the ovarian cells in supplementary Fig. S3, which showed large differences in the AFM and consistent results in the KPFM plots. This demonstrates the advantage of the KPFM method for cancer detection compared to AFM. This is because AFM is more sensitive to ambient dust contamination that introduces large random height fluctuations, while KPFM measures bioelectric signals, which are less sensitive to random height fluctuations from the occasional uncharged particles.

Supplementary Fig. S4 shows typical representative AFM and KPFM profiles that were obtained by averaging 5 lines of the $3 \times 3 \mu\text{m}^2$ scan areas used in the multifractal analysis. The profiles show the amplitude and correlation between fluctuations of height (AFM) and surface potential (KPFM) of normal and cancer cells. The linear correlation coefficients between the AFM and KPFM profiles of MCF-10A, MDA-MB-231, SHT290, and ES-2 cells are 0.696, 0.434, 0.038, and 0.362, respectively. The results show larger spatial fluctuations of surface potential of cancer cells compared to normal cells, characterized by fractal and multifractal analyses.

Fractal analysis

First, we present the results of fractal analysis of AFM and KPFM images using the box-counting method with adaptive thresholding. Figure 2 shows the dependence of the local fractal dimension D_f as a function of the box size r that was obtained from the slope of the tangent of $N(r)$ at each value of r estimated from the box-counting algorithm ($D_f = -d \ln N(r) / d \ln r$) [58]. Thick solid lines correspond to the mean values, while thin dashed lines show individual cell data. The supplementary Fig. S5 shows the corresponding results using the median threshold analysis. These

figures show similar average trends as the examples of the individual cells described above. KPFM shows more consistent results compared to AFM due to the smaller sensitivity to random particles.

The main insight from the fractal analysis in Fig. 2 is the observation that the local fractal dimension is not constant over the range of box sizes and varies for the different cell lines. This leads to the conclusion that both AFM and KPFM images cannot be described as simple fractal objects. They have a more complex organization that depends on the scaling range. This requires the multifractal analysis shown below. However, fractal analysis can still be used to distinguish normal and cancer cells. It can show general trends in the variations of the local height and surface potential. For example, Fig. 2a shows smaller cell-to-cell variations in AFM local dimensions for MDA-MB-231 cells (red dashed lines) compared to MCF-10A cells (blue dashed lines). This indicates that MDA-MB-231 cell topography is closer to being fractal than MCF-10A. MDA-MB-231 cell height variations may be approximately described by a fractal dimension of ~ 1.9 , while the fractal dimension of MCF-10A cells varies widely within $\sim 1.5 - 2$ range. KPFM images show similar trends with different fractal dimensions. A smaller average range of local fractal dimensions of $\sim 1.6 - 2$ for MDA-MB-231 cells (thick solid red line in Fig. 2b) indicates a more fractal-like description compared to the broader average range of $\sim 1.5 - 2$ for MCF-10A cells (thick solid blue line in Fig. 2b). Overall, both breast and ovarian cell lines exhibited a loss of multifractality upon cancerous transformation that is confirmed by the multifractal analysis below. Also, KPFM data for MDA-MB-231 cells (red dashed lines in Fig. 2b) show larger cell-to-cell variations compared to MCF-10A cells. This reflects a larger heterogeneity of the surface potential of cancer cells compared to normal cells.

The AFM fractal analysis of the ovarian cells in Fig. 2c shows similar trends, which are unable to distinguish between the normal and cancer cells. On the other hand, KPFM shows a better distinguishability in Fig. 2d. Overall, although fractal analysis can be used to distinguish between the normal and cancer cells, it provides limited insights into the multiscale organization of the morphology and surface potential.

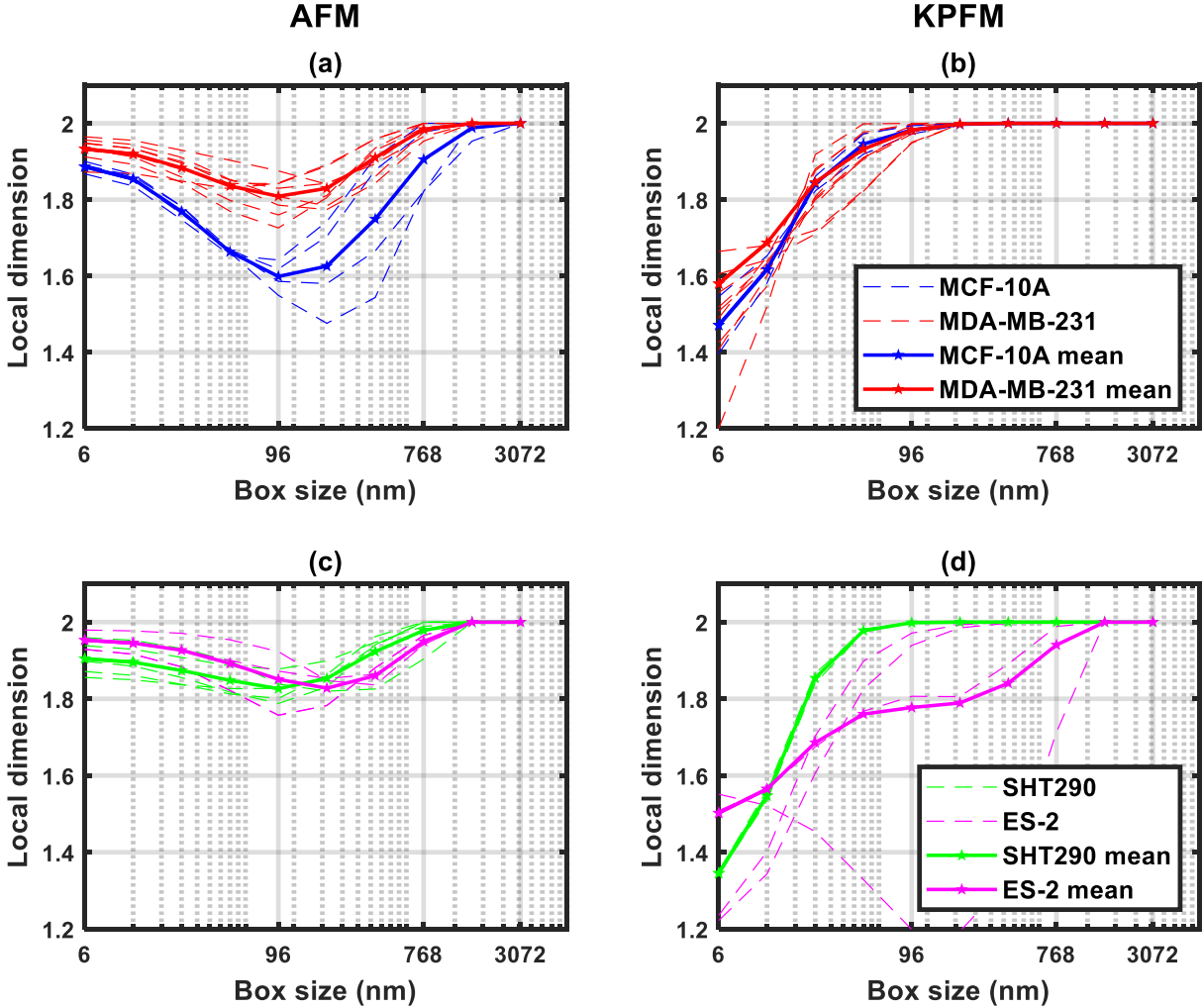


Figure 2. Fractal analysis of AFM and KPFM images using the box-counting method with adaptive thresholding. Dependence of the local fractal dimension D_f as a function of the box size for individual cells (thin dashed lines) and mean data (thick solid lines).

Multifractal analysis

Next, we performed multifractal analysis of the same AFM and KPFM images of the four cell lines that were used for the fractal analysis above. Figure 3 shows the Rényi spectra D_q , multifractal spectra $f(\alpha)$, and singularity width $\Delta\alpha$ obtained using the adaptive method. Thick solid lines show the averages over all areas of the cells including both cytoplasm and nucleus. Thin dashed lines show individual areas. The corresponding results using the median method are shown in supplementary Fig. S6.

The Rényi spectra in Figs. 3a – 3d show significant differences between the normal and cancer cells at D_1 and D_2 values (vertical dashed lines) in KPFM compared to AFM images. In these plots, positive q values accentuate denser regions, and negative q accentuate the less dense regions. On the contrary, the Rényi spectra show larger differences between the normal and cancer cells at D_0 for AFM compared to KPFM. These results are summarized in Tables 1 and 2 below. The median method did not give satisfactory results for AFM images (see supplementary Figs. S6a and S6c). However, it showed satisfactory results for the KPFM images (supplementary Figs. S6b and S6d), confirming the conclusion from the fractal analysis that surface potential is less sensitive than topography to random height variations.

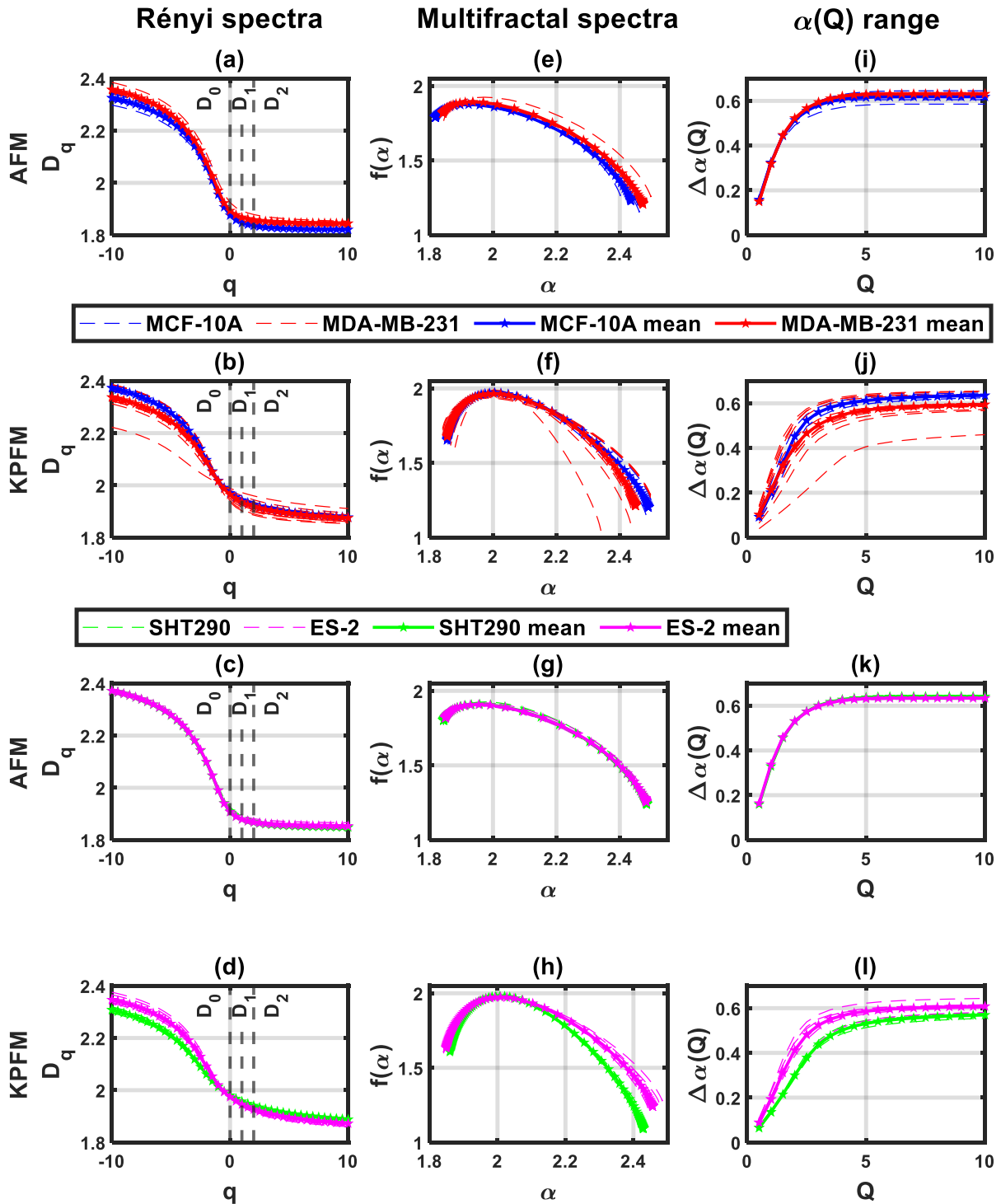


Figure 3. Rényi spectra (a – d), multifractal spectra (e - h), and singularity exponent range (i - l) obtained from multifractal analysis of adaptive AFM and KPFM images of normal and cancer cells for individual areas (dashed lines) and averages (solid lines). Vertical dashed lines mark the D_0 , D_1 and D_2 values.

The multifractal spectra in Figs. 3e – 3h provide direct information about the multifractality of AFM and KPFM images. The concave shape of the spectra indicates multifractality, which is quantified by the width $\Delta\alpha$. The wider spectra with the larger $\Delta\alpha$ correspond to higher multifractality. Figure 3e shows multifractal spectra for AFM images of breast cells that have similar width $\Delta\alpha$ but different D_0 , i. e. the MDA-MB-231 spectra (red lines) are shifted to higher α values. The corresponding KPFM spectra in Fig. 3f show similar shapes with similar D_0 and $\Delta\alpha$ parameters. The KPFM spectra in Fig. 3f cannot distinguish between the normal and cancer cells, but they quantify multifractality and provide further insights to support the results of fractal analysis in Fig. 2.

Multifractal analysis of the ovarian cells showed qualitatively different results. While no significant difference was observed in the AFM spectra (Fig. 3g), there was a significant difference in the width $\Delta\alpha$ of ES-2 cells (magenta lines) having larger $\Delta\alpha$ than SHT290 (green lines) as shown in Fig. 3h. Also, AFM spectra of both ES-2 and SHT290 cells showed small cell-to-cell variations in the whole α range in Fig. 3g, while KPFM spectra showed larger variations for ES-2 compared to SHT290 at large α values (Fig. 3h). This indicates heterogeneity of the cancer cell surface potential despite the small variations in cell morphology.

We compared the adaptive and median image binarization methods for fractal and multifractal analyses. The adaptive method showed standard concave $f(\alpha)$ curves for both AFM and KPFM images, while the median method failed. The adaptive method showed statistically significant differences between the KPFM multifractality for the ovarian cancer cells but the corresponding analysis using the median method showed large errors and non-concave $f(\alpha)$ curve shapes for AFM.

The main result in Figs. 3g and 3h is that the surface potential of cancer cells is more multifractal compared to normal cells. Multifractality is more pronounced at large values of the momentum Q as shown in the Methods sections. Figures 3i – 3l show the $\Delta\alpha(Q)$ plots to better visualize multifractality at different Q values. Figs. 3k and 3l show a drastic difference between the multifractality changes of AFM and KPFM images of the ovarian cells. It supports the conclusion that $\Delta\alpha$ of surface potential can be used as a cancer biomarker.

Figure 4 shows the comparison of the parameters D_0 , D_1 , D_2 , and $\Delta\alpha(4)$ from the cytoplasm, nucleus, and combined regions using adaptive method. The corresponding results using the median method are shown in supplementary Fig. S7. Figs. 4a, 4c and 4d show that D_0 , D_1 , and D_2 of the

AFM images of MCF-10A are lower than that of MDA-MB-231 (D_0 at $p < 0.05$; D_1 at $p < 0.01$; D_2 at $p < 0.001$; see Table 1). This indicates the increase of the morphological local fractal dimension and heterogeneity (disorder) in breast cancer cells. Fig. 4b shows no significant difference in the mean value of $\Delta\alpha(4)$ of the AFM images of the four cell types but MCF-10A cells showed the largest variance of $\Delta\alpha(4)$.

Figure 4 shows the opposite behavior of the AFM and KPFM multifractal parameters. In particular, Figs. 4e, 4g and 4h show that D_0, D_1 , and D_2 of KPFM images of SHT290 are larger than those of ES-2 ($p < 0.1$; Table 2), which indicates the lower local fractal dimension of surface potential in ovarian cancer cells compared to normal endometrial cells. However, the D_0, D_1 , and D_2 parameters have larger variations for ES-2 compared to SHT290 cells, possibly reflecting a larger heterogeneity of the cancer cells. Fig. 4f shows a larger mean value of $\Delta\alpha(4)$ for ES-2 compared to SHT290 ($p < 0.05$), indicating larger multifractality of the ovarian cancer cell surface potential. No significant difference between the mean values of the surface potential $\Delta\alpha(4)$ were found for MCF-10A and MDA-MB-231 cells. However, the MDA-MB-231 cells showed larger variations of $\Delta\alpha(4)$.

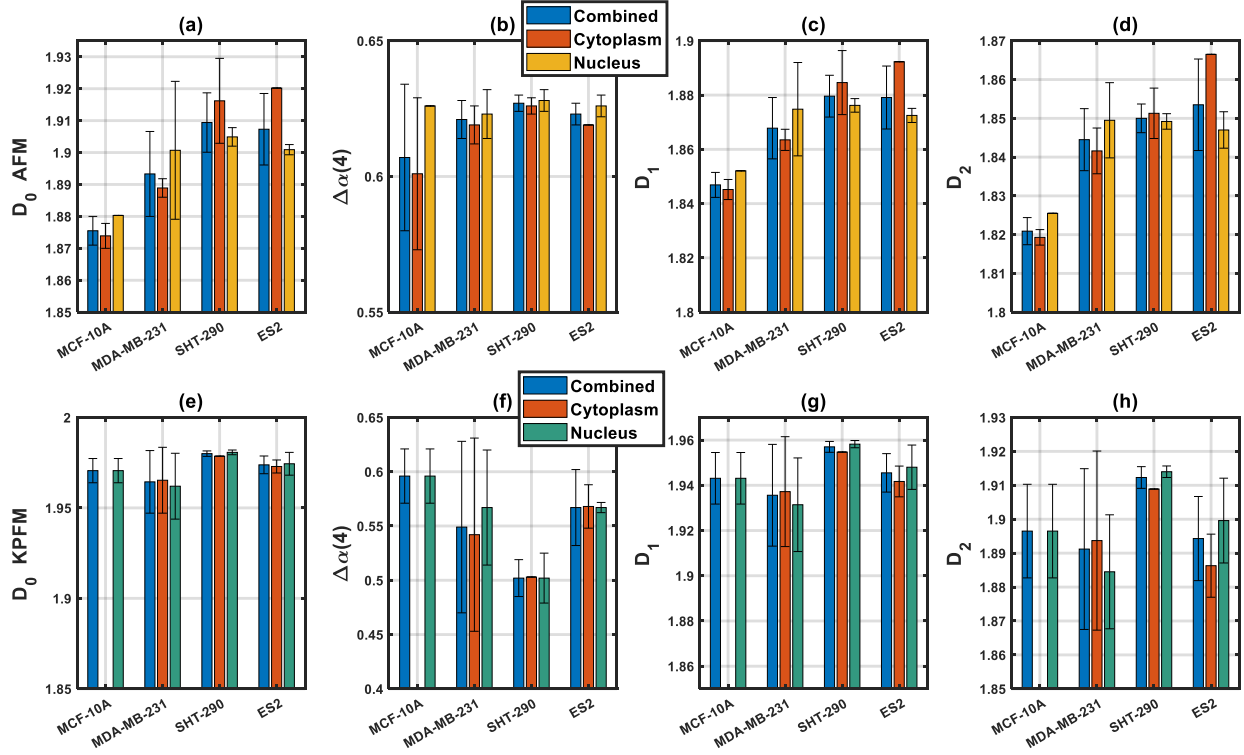


Figure 4. Comparison of the multifractal parameters D_0 , D_1 , D_2 , and $\Delta\alpha(4)$ from the combined and separate cytoplasm and nucleus regions using adaptive method.

The hypothesis testing results for the differences in the multifractal parameters of AFM and KPFM images using the adaptive method are shown in Tables 1 and 2. The hypothesis testing for the mean difference in the multifractal parameters of AFM images revealed the significant differences in D_0 , D_1 , and D_2 between the MCF-10A and MDA-MB-231 cell lines at the significance level of 0.05, but no significant difference in $\Delta\alpha(4)$ was found (Table 1). However, for the ovarian cell lines, no significant differences in the four multifractal parameters of the AFM images of SHT290 and ES-2 cell lines were identified.

Table 1. Hypothesis testing for the difference in the multifractal parameters (box counting dimension D_0 , entropy dimension D_1 , correlation dimension D_2 , and singularity exponent range $\Delta\alpha(4)$) of AFM images using the adaptive method.

Hypothesis testing	Sample pair	$\bar{X}_1 \pm s_1$	$\bar{X}_2 \pm s_2$	p-value
Mean difference in D_0	MCF-10A vs MDA-MB-231	1.876 ± 0.005	1.894 ± 0.013	0.0286 ^{***a}
	SHT290 vs ES-2	1.909 ± 0.009	1.907 ± 0.011	0.7801
Mean difference in D_1	MCF-10A vs MDA-MB-231	1.847 ± 0.005	1.868 ± 0.011	0.0059 ^{**}
	SHT290 vs ES-2	1.880 ± 0.008	1.880 ± 0.012	0.9429
Mean difference in D_2	MCF-10A vs MDA-MB-231	1.821 ± 0.004	1.845 ± 0.008	0.0002 ^{**}
	SHT290 vs ES-2	1.850 ± 0.004	1.854 ± 0.012	0.5434
Mean difference in $\Delta\alpha(4)$	MCF-10A vs MDA-MB-231	0.607 ± 0.027	0.621 ± 0.007	0.1793
	SHT290 vs ES-2	0.627 ± 0.003	0.623 ± 0.004	0.1615

^aSignificance codes: $p < 0.001$ ‘****’, $p < 0.01$ ‘***’, $p < 0.05$ ‘*’

In contrast to the hypothesis testing results of the AFM images, the hypothesis tests for the KPFM images mean difference in D_0 , D_1 , and D_2 showed the significant differences between the SHT290 and ES-2 cell lines at the significance level of 0.1 and the significant difference in $\Delta\alpha(4)$ at the level of 0.05, but there were no significant differences between MCF-10A and MDA-MB-231 cell lines in terms of the four multifractal parameters (Table 2).

Table 2. Hypothesis testing for the difference in the multifractal parameters (box counting dimension D_0 , entropy dimension D_1 , correlation dimension D_2 , and singularity exponent range $\Delta\alpha(4)$) of KPFM images using the adaptive method.

Hypothesis testing	Sample pair	$\bar{X}_1 \pm s_1$	$\bar{X}_2 \pm s_2$	p-value ^a
Mean difference in D_0	MCF-10A vs MDA-MB-231	1.971 ± 0.007	1.964 ± 0.017	0.6354
	SHT290 vs ES-2	1.980 ± 0.002	1.974 ± 0.005	0.0821 ·
Mean difference in D_1	MCF-10A vs MDA-MB-231	1.943 ± 0.011	1.936 ± 0.023	0.6645
	SHT290 vs ES-2	1.957 ± 0.002	1.946 ± 0.009	0.0656 ·
Mean difference in D_2	MCF-10A vs MDA-MB-231	1.897 ± 0.014	1.845 ± 0.008	0.7685
	SHT290 vs ES-2	1.912 ± 0.003	1.894 ± 0.012	0.0536 ·
Mean difference in $\Delta\alpha(4)$	MCF-10A vs MDA-MB-231	0.596 ± 0.025	0.549 ± 0.079	0.4339
	SHT290 vs ES-2	0.502 ± 0.017	0.567 ± 0.035	0.0256*

^aSignificance codes: $p < 0.05$ ‘*’, $p < 0.1$ ‘·’

4. DISCUSSION

The observed differences between the morphological and surface potential measurements can be explained by the molecular structural and bioelectric changes of the plasma membrane. Our results suggest that AFM and KPFM are complementary imaging techniques that reflect different molecular mechanisms of tumorigenesis, such as the expression of membrane surface proteins, activity of ion channels and cytoskeletal reorganization. In the case of ovarian cancer cells (*i.e.*, normal-immortalized SHT290 and tumorigenic ES-2), KPFM provides significant differences in multifractality, while AFM does not. These observations agree with the molecular model of ovarian cancer based on the overexpression of certain proteins such as the protein kinase C (PKC) family [59, 60]. PKC activation by Ca^{2+} may reflect the change in the surface potential. Although binding of PKC to the inner side of the plasma membrane does not affect the membrane outer surface morphology [60]. The previous study showed an overexpression of PKC proteins in ES-2 cells compared to SHT290 cells [60], it utilizes Ca^{2+} in a complex signaling cascade involved in cancer progression. Similar importance of PKC proteins was previously shown in breast cancer [61-63]. Overexpression of PKC- ξ protein was previously correlated with the invasiveness in MDA-MB-231 cells [63]. In addition, the PKC signaling pathway effects cytoskeleton reorganization by regulating the actin polymerization, lipid metabolism and Ca^{2+} [64]. These and other morphological changes may be responsible for the differences that we observed in the AFM fractality of breast cells.

Previous studies reported a depolarization of the surface potential of cancer cells and tissues [5, 6]. Although ovarian ES-2/SHT290 cells exhibited a larger depolarization compared to breast MCF-10A/MDA-MB-231, of note is the higher variance among both tissue types in the cancerous cell lines compared to their normal-immortalized counterparts. The smaller size of the ovarian ($\sim 10\text{-}15\ \mu\text{m}$) compared to breast ($\sim 20\text{-}30\ \mu\text{m}$) and the small sample size may be the reason that our results on multifractality did not show a significant difference between the MCF-10A and MDA-MB-231 cells. Based on the larger difference in surface potential, we predict that the multifractal method may also work well on pancreatic, hepatic, and rectal cancer.

Note that our imaging was performed under steady-state conditions, in which the sub-millisecond temporal fluctuations of surface potential were averaged out. Therefore, our work is focused on spatial fluctuations. Recent work on temporal dynamics of the surface potential revealed larger fluctuations in MDA-MB-231 cells compared to MCF-10A cells [65]. Although

potential fluctuations in cancer cells were inhibited by the voltage-gated Na channel and Ca²⁺-activated K channel blockers, which indicates the possible role of the ion channels in modifying the membrane morphology that we measured in our AFM experiments. However, the previous measurements in [65] were performed using voltage-sensitive dyes and were not label-free. Our KPFM measurements, on the other hand, are label-free and are minimally invasive.

The comparison between the nucleus and cytoplasm areas did not show any significant differences in both AFM and KPFM signals, indicating that the cell migration mechanisms of cytoskeletal reorganization do not contribute to the observed multifractality of surface potential. For example, Ca²⁺ flickering was previously found to be predominant in lamellipodia at migrating cell edges [66]. High calcium microdomains were observed that could contribute to the spatial organization of surface potential and polarity between the leading and trailing edges. However, our study included both edges and showed no significant differences, ruling out the calcium-based migration mechanism.

To the best of our knowledge, our work shows multifractality in surface potential of biological cells for the first time. Fractal and multifractal potentials may lead to large fluctuations of local electric fields, such as electric hot spots in nanoplasmonics systems used for sensing applications [67-69]. Large electric fields in biological cell systems may be attributed to fractal aggregation of charged proteins [70] accompanied by complex heterogeneous potential landscapes [71, 72].

5. CONCLUSION

In summary, we measured the surface potential of normal and cancer cells with nanoscale resolution. We used fractal and multifractal analysis to characterize the time-averaged spatial potential fluctuations and observed changes in multifractality of ES-2 ovarian cancer cells compared to control SHT290 normal endometrial cells. The ovarian cancer cells had a more multifractal surface potential compared to the normal cells. While AFM morphology failed to distinguish between normal and cancer cells, we observed multifractality in the surface potential of breast cancer cells, which, however, did not show a significant difference from the normal breast cells. We observed significant differences in the AFM morphological fractal dimension of these non-malignant and malignant breast cells. Based on the comparison between the morphological and surface potential images of normal and cancer cells, we conclude that the combination of these two imaging techniques improves cancer detection by providing complementary information. Cell

functions such as immune signaling, metabolism and apoptosis are dysregulated during tumor growth, resulting in catastrophic physical and bioelectric changes that can be characterized by the multifractality of the AFM and KPFM images. The characterized morphological and surface potential images will facilitate our previous works on probabilistic modeling of disorder pathogenesis [73-75] by adding more details from cell and tissue levels. Multifractality in surface potential can also be used as a novel biomarker for novel drug delivery methods based on bioelectric activation.

DECLARATION OF COMPETING INTERESTS

The authors declare that they have no known competing financial interests or personal relationships that could have appeared to influence the work reported in this paper.

REFERENCES

- [1] S. Pecorelli, G. Favalli, L. Zigliani, and F. Odicino, "Cancer in women," *International Journal of Gynecology & Obstetrics*, vol. 82, no. 3, pp. 369-379, 2003.
- [2] Z. Momenimovahed, A. Tiznobaik, S. Taheri, and H. Salehiniya, "Ovarian cancer in the world: epidemiology and risk factors," *International journal of women's health*, pp. 287-299, 2019.
- [3] S. De Silva, K. H. Tennekoon, and E. H. Karunanayake, "Overview of the genetic basis toward early detection of breast cancer," *Breast Cancer: Targets and Therapy*, pp. 71-80, 2019.
- [4] B. Chernet and M. Levin, "Endogenous voltage potentials and the microenvironment: bioelectric signals that reveal, induce and normalize cancer," *Journal of clinical & experimental oncology*, 2013.
- [5] M. Yang and W. J. Brackenbury, "Membrane potential and cancer progression," *Frontiers in physiology*, vol. 4, p. 185, 2013.
- [6] H. Zhao, W. Zhang, X. Tang, E. A. Galan, Y. Zhu, G. Sang, D. Khutsishvili, H. Zheng, and S. Ma, "Electrostatic potential difference between tumor and paratumor regulates cancer stem cell behavior and prognose tumor spread," *Bioengineering & Translational Medicine*, p. e10399, 2022.
- [7] W. Melitz, J. Shen, A. C. Kummel, and S. Lee, "Kelvin probe force microscopy and its application," *Surface science reports*, vol. 66, no. 1, pp. 1-27, 2011.

- [8] J. Park, J. Yang, G. Lee, C. Y. Lee, S. Na, S. W. Lee, S. Haam, Y.-M. Huh, D. S. Yoon, and K. Eom, "Single-molecule recognition of biomolecular interaction via Kelvin probe force microscopy," *ACS nano*, vol. 5, no. 9, pp. 6981-6990, 2011.
- [9] G. Lee, W. Lee, H. Lee, S. Woo Lee, D. Sung Yoon, K. Eom, and T. Kwon, "Mapping the surface charge distribution of amyloid fibril," *Applied Physics Letters*, vol. 101, no. 4, p. 043703, 2012.
- [10] W. Lee, H. Jung, M. Son, H. Lee, T. J. Kwak, G. Lee, C. H. Kim, S. W. Lee, and D. S. Yoon, "Characterization of the regrowth behavior of amyloid-like fragmented fibrils decomposed by ultrasonic treatment," *RSC Advances*, vol. 4, no. 100, pp. 56561-56566, 2014.
- [11] C. Leung, D. Maradan, A. Kramer, S. Howorka, P. Mesquida, and B. W. Hoogenboom, "Improved Kelvin probe force microscopy for imaging individual DNA molecules on insulating surfaces," *Applied Physics Letters*, vol. 97, no. 20, p. 203703, 2010.
- [12] D. N. Richards, D. Y. Zemlyanov, R. M. Asrar, Y. Y. Chokshi, E. M. Cook, T. J. Hinton, X. Lu, V. Q. Nguyen, N. K. Patel, and J. R. Usher, "DNA immobilization on GaP (100) investigated by kelvin probe force microscopy," *The Journal of Physical Chemistry C*, vol. 114, no. 36, pp. 15486-15490, 2010.
- [13] H. Lee, W. Lee, J. H. Lee, and D. S. Yoon, "Surface potential analysis of nanoscale biomaterials and devices using kelvin probe force microscopy," *Journal of Nanomaterials*, vol. 2016, 2016.
- [14] P. Gao and Y. Cai, "Label-free detection of the aptamer binding on protein patterns using Kelvin probe force microscopy (KPFM)," *Analytical and bioanalytical chemistry*, vol. 394, no. 1, pp. 207-214, 2009.
- [15] C.-C. Tsai, H.-H. Hung, C.-P. Liu, Y.-T. Chen, and C.-Y. Pan, "Changes in plasma membrane surface potential of PC12 cells as measured by Kelvin probe force microscopy," *PLoS One*, vol. 7, no. 4, p. e33849, 2012.
- [16] W. Zhao, W. Cui, S. Xu, L.-Z. Cheong, D. Wang, and C. Shen, "Direct study of the electrical properties of PC12 cells and hippocampal neurons by EFM and KPFM," *Nanoscale Advances*, vol. 1, no. 2, pp. 537-545, 2019.
- [17] H. Lee, S. W. Lee, G. Lee, W. Lee, J. H. Lee, K. S. Hwang, J. Yang, S. W. Lee, and D. S. Yoon, "Kelvin probe force microscopy of DNA-capped nanoparticles for single-nucleotide polymorphism detection," *Nanoscale*, vol. 8, no. 28, pp. 13537-13544, 2016.

- [18] K. Jang, J. Choi, C. Park, and S. Na, "Label-free and high-sensitive detection of Kirsten rat sarcoma viral oncogene homolog and epidermal growth factor receptor mutation using Kelvin probe force microscopy," *Biosensors and Bioelectronics*, vol. 87, pp. 222-228, 2017.
- [19] T. Kwon, S. Gunasekaran, and K. Eom, "Atomic force microscopy-based cancer diagnosis by detecting cancer-specific biomolecules and cells," *Biochimica et Biophysica Acta (BBA)-Reviews on Cancer*, vol. 1871, no. 2, pp. 367-378, 2019.
- [20] J. Zemła, J. Danilkiewicz, B. Orzechowska, J. Pabijan, S. Seweryn, and M. Lekka, "Atomic force microscopy as a tool for assessing the cellular elasticity and adhesiveness to identify cancer cells and tissues," in *Seminars in cell & developmental biology*, 2018, vol. 73: Elsevier, pp. 115-124.
- [21] X. Deng, F. Xiong, X. Li, B. Xiang, Z. Li, X. Wu, C. Guo, X. Li, Y. Li, and G. Li, "Application of atomic force microscopy in cancer research," *Journal of nanobiotechnology*, vol. 16, no. 1, pp. 1-15, 2018.
- [22] L. Bemmerlein, I. A. Deniz, J. Karbanová, A. Jacobi, S. Drukewitz, T. Link, A. Göbel, L. Sevenich, A. V. Taubenberger, and P. Wimberger, "Decoding Single Cell Morphology in Osteotropic Breast Cancer Cells for Dissecting Their Migratory, Molecular and Biophysical Heterogeneity," *Cancers*, vol. 14, no. 3, p. 603, 2022.
- [23] S. E. Cross, Y.-S. Jin, J. Tondre, R. Wong, J. Rao, and J. K. Gimzewski, "AFM-based analysis of human metastatic cancer cells," *Nanotechnology*, vol. 19, no. 38, p. 384003, 2008.
- [24] M. E. Dokukin, N. V. Guz, R. M. Gaikwad, C. D. Woodworth, and I. Sokolov, "Cell surface as a fractal: normal and cancerous cervical cells demonstrate different fractal behavior of surface adhesion maps at the nanoscale," *Physical review letters*, vol. 107, no. 2, p. 028101, 2011.
- [25] E. Bakalis, A. Ferraro, V. Gavriil, F. Pepe, Z. Kollia, A.-C. Cefalas, U. Malapelle, E. Sarantopoulou, G. Troncone, and F. Zerbetto, "Universal Markers Unveil Metastatic Cancerous Cross-Sections at Nanoscale," *Cancers*, vol. 14, no. 15, p. 3728, 2022.
- [26] A. Mezheyeuski, I. Hrynchyk, M. Karlberg, A. Portyanko, L. Egevad, P. Ragnhammar, D. Edler, B. Glimelius, and A. Östman, "Image analysis-derived metrics of histomorphological complexity predicts prognosis and treatment response in stage II-III colon cancer," *Scientific reports*, vol. 6, no. 1, pp. 1-9, 2016.

- [27] F. E. Lennon, G. C. Cianci, N. A. Cipriani, T. A. Hensing, H. J. Zhang, C.-T. Chen, S. D. Murgu, E. E. Vokes, M. W. Vannier, and R. Salgia, "Lung cancer—a fractal viewpoint," *Nature reviews Clinical oncology*, vol. 12, no. 11, pp. 664-675, 2015.
- [28] M. Bizzarri, A. Giuliani, A. Cucina, F. D'Anselmi, A. M. Soto, and C. Sonnenschein, "Fractal analysis in a systems biology approach to cancer," in *Seminars in cancer biology*, 2011, vol. 21, no. 3: Elsevier, pp. 175-182.
- [29] P. Kestener, J. M. Lina, P. Saint-Jean, and A. Arneodo, "Wavelet-based multifractal formalism to assist in diagnosis in digitized mammograms," *Image Analysis & Stereology*, vol. 20, no. 3, pp. 169-174, 2001.
- [30] N. V. Guz, M. E. Dokukin, C. D. Woodworth, A. Cardin, and I. Sokolov, "Towards early detection of cervical cancer: Fractal dimension of AFM images of human cervical epithelial cells at different stages of progression to cancer," *Nanomedicine: Nanotechnology, Biology and Medicine*, vol. 11, no. 7, pp. 1667-1675, 2015.
- [31] R. Lopes and N. Betrouni, "Fractal and multifractal analysis: a review," *Medical image analysis*, vol. 13, no. 4, pp. 634-649, 2009.
- [32] J. d. D. H. Velázquez, S. Mejía-Rosales, and A. G. Goicochea, "Fractal properties of biophysical models of pericellular brushes can be used to differentiate between cancerous and normal cervical epithelial cells," *Colloids and Surfaces B: Biointerfaces*, vol. 170, pp. 572-577, 2018.
- [33] R. Sedivy and R. M. Mader, "Fractals, chaos, and cancer: do they coincide?," *Cancer investigation*, vol. 15, no. 6, pp. 601-607, 1997.
- [34] J. W. Baish and R. K. Jain, "Fractals and cancer," *Cancer research*, vol. 60, no. 14, pp. 3683-3688, 2000.
- [35] B. B. Mandelbrot, *Multifractals and 1/f noise: Wild self-affinity in physics (1963–1976)*. Springer, 2013.
- [36] Q. Cheng, "Multifractality and spatial statistics," *Computers & Geosciences*, vol. 25, no. 9, pp. 949-961, 1999.
- [37] C. S. Barbier, K. A. Becker, M. A. Troester, and D. G. Kaufman, "Expression of exogenous human telomerase in cultures of endometrial stromal cells does not alter their hormone responsiveness," *Biology of reproduction*, vol. 73, no. 1, pp. 106-114, 2005.

- [38] L. Hayflick and P. S. Moorhead, "The serial cultivation of human diploid cell strains," *Experimental cell research*, vol. 25, no. 3, pp. 585-621, 1961.
- [39] H. D. Soule, T. M. Maloney, S. R. Wolman, W. D. Peterson Jr, R. Brenz, C. M. McGrath, J. Russo, R. J. Pauley, R. F. Jones, and S. Brooks, "Isolation and characterization of a spontaneously immortalized human breast epithelial cell line, MCF-10," *Cancer research*, vol. 50, no. 18, pp. 6075-6086, 1990.
- [40] H. Soule, J. Vazquez, A. Long, S. Albert, and M. Brennan, "A human cell line from a pleural effusion derived from a breast carcinoma," *Journal of the national cancer institute*, vol. 51, no. 5, pp. 1409-1416, 1973.
- [41] S. Takeda, S. Okajima, H. Miyoshi, K. Yoshida, Y. Okamoto, T. Okada, T. Amamoto, K. Watanabe, C. J. Omiecinski, and H. Aramaki, "Cannabidiolic acid, a major cannabinoid in fiber-type cannabis, is an inhibitor of MDA-MB-231 breast cancer cell migration," *Toxicology letters*, vol. 214, no. 3, pp. 314-319, 2012.
- [42] R. Cailleau, M. Olive, and Q. V. Cruciger, "Long-term human breast carcinoma cell lines of metastatic origin: preliminary characterization," *In vitro*, vol. 14, no. 11, pp. 911-915, 1978.
- [43] S. Huang and D. E. Ingber, "The structural and mechanical complexity of cell-growth control," *Nature cell biology*, vol. 1, no. 5, pp. E131-E138, 1999.
- [44] D. Bradley and G. Roth, "Adaptive thresholding using the integral image," *Journal of graphics tools*, vol. 12, no. 2, pp. 13-21, 2007.
- [45] B. B. Mandelbrot, *The fractal geometry of nature*. WH freeman New York, 1982.
- [46] M. Wu, W. Wang, D. Shi, Z. Song, M. Li, and Y. Luo, "Improved box-counting methods to directly estimate the fractal dimension of a rough surface," *Measurement*, vol. 177, p. 109303, 2021.
- [47] M. Ge and Q. Lin, "Realizing the box-counting method for calculating fractal dimension of urban form based on remote sensing image," *Geo-spatial Information science*, vol. 12, no. 4, pp. 265-270, 2009.
- [48] A. N. Posadas, D. Giménez, R. Quiroz, and R. Protz, "Multifractal characterization of soil pore systems," *Soil Science Society of America Journal*, vol. 67, no. 5, pp. 1361-1369, 2003.
- [49] B. Yao, F. Imani, A. S. Sakpal, E. Reutzler, and H. Yang, "Multifractal analysis of image profiles for the characterization and detection of defects in additive manufacturing," *Journal of Manufacturing Science and Engineering*, vol. 140, no. 3, 2018.

- [50] G. F. Grosu, A. V. Hopp, V. V. Moca, H. Bârzan, A. Ciuparu, M. Ercsey-Ravasz, M. Winkel, H. Linde, and R. C. Mureşan, "The fractal brain: scale-invariance in structure and dynamics," *Cerebral Cortex*, 2022.
- [51] E. Ge and Y. Leung, "Detection of crossover time scales in multifractal detrended fluctuation analysis," *Journal of Geographical Systems*, vol. 15, no. 2, pp. 115-147, 2013.
- [52] T. Thomas and B.-G. Rosén, "Implementation of Whitehouse's method for calculating properties of self-affine fractal profiles," *Proceedings of the Institution of Mechanical Engineers, Part C: Journal of Mechanical Engineering Science*, vol. 222, no. 8, pp. 1547-1550, 2008.
- [53] B. B. Mandelbrot, "Multifractal measures, especially for the geophysicist," in *Fractals in geophysics*: Springer, 1989, pp. 5-42.
- [54] M. I. Hwang and J. W. Lin, "Information dimension, information overload and decision quality," *Journal of information science*, vol. 25, no. 3, pp. 213-218, 1999.
- [55] J. C. Sprott and G. Rowlands, "Improved correlation dimension calculation," *International Journal of Bifurcation and Chaos*, vol. 11, no. 07, pp. 1865-1880, 2001.
- [56] J. Lafond, L. Han, S. Allaire, and P. Dutilleul, "Multifractal properties of porosity as calculated from computed tomography (CT) images of a sandy soil, in relation to soil gas diffusion and linked soil physical properties," *European Journal of Soil Science*, vol. 63, no. 6, pp. 861-873, 2012.
- [57] P. Jizba and T. Arimitsu, "The world according to Rényi: thermodynamics of multifractal systems," *Annals of Physics*, vol. 312, no. 1, pp. 17-59, 2004.
- [58] Y. Liu, L. Chen, H. Wang, L. Jiang, Y. Zhang, J. Zhao, D. Wang, Y. Zhao, and Y. Song, "An improved differential box-counting method to estimate fractal dimensions of gray-level images," *Journal of visual communication and Image Representation*, vol. 25, no. 5, pp. 1102-1111, 2014.
- [59] E. M. Griner and M. G. Kazanietz, "Protein kinase C and other diacylglycerol effectors in cancer," *Nature Reviews Cancer*, vol. 7, no. 4, pp. 281-294, 2007.
- [60] T. Smalley, R. Metcalf, R. Patel, S. A. Islam, R. R. Bommareddy, and M. Acevedo-Duncan, "The atypical protein kinase c small molecule inhibitor ζ -stat, and its effects on invasion through decreases in pkc- ζ protein expression," *Frontiers in Oncology*, vol. 10, p. 209, 2020.

- [61] T. Hirai and K. Chida, "Protein kinase C ζ (PKC ζ): activation mechanisms and cellular functions," *Journal of biochemistry*, vol. 133, no. 1, pp. 1-7, 2003.
- [62] A. Paul, M. Danley, B. Saha, O. Tawfik, and S. Paul, "PKC ζ promotes breast cancer invasion by regulating expression of E-cadherin and Zonula Occludens-1 (ZO-1) via NF κ B-p65," *Scientific reports*, vol. 5, no. 1, pp. 1-17, 2015.
- [63] T. Smalley, S. Islam, C. Apostolatos, A. Apostolatos, and M. Acevedo-Duncan, "Analysis of PKC- ζ protein levels in normal and malignant breast tissue subtypes," *Oncology Letters*, vol. 17, no. 2, pp. 1537-1546, 2019.
- [64] S. Kouba, L. Ouldamer, C. Garcia, D. Fontaine, A. Chantome, C. Vandier, C. Goupille, and M. Potier-Cartereau, "Lipid metabolism and Calcium signaling in epithelial ovarian cancer," *Cell calcium*, vol. 81, pp. 38-50, 2019.
- [65] P. Quicke, Y. Sun, M. Arias-Garcia, M. Beykou, C. D. Acker, M. B. Djamgoz, C. Bakal, and A. J. Foust, "Voltage imaging reveals the dynamic electrical signatures of human breast cancer cells," *Communications Biology*, vol. 5, no. 1, p. 1178, 2022.
- [66] C. Wei, X. Wang, M. Chen, K. Ouyang, L.-S. Song, and H. Cheng, "Calcium flickers steer cell migration," *Nature*, vol. 457, no. 7231, pp. 901-905, 2009.
- [67] V. M. Shalaev, *Nonlinear optics of random media: fractal composites and metal-dielectric films*. Springer Science & Business Media, 1999.
- [68] V. Markel, L. Muratov, M. I. Stockman, and T. F. George, "Theory and numerical simulation of optical properties of fractal clusters," *Physical Review B*, vol. 43, no. 10, p. 8183, 1991.
- [69] K. Li, M. I. Stockman, and D. J. Bergman, "Self-similar chain of metal nanospheres as an efficient nanolens," *Physical review letters*, vol. 91, no. 22, p. 227402, 2003.
- [70] E. Baskin and A. Iomin, "Electrostatics in fractal geometry: fractional calculus approach," *Chaos, Solitons & Fractals*, vol. 44, no. 4-5, pp. 335-341, 2011.
- [71] V. P. Andreev, "Cytoplasmic electric fields and electroosmosis: possible solution for the paradoxes of the intracellular transport of biomolecules," *PloS one*, vol. 8, no. 4, p. e61884, 2013.
- [72] K. M. Tyner, R. Kopelman, and M. A. Philbert, "'Nanosized voltmeter' enables cellular-wide electric field mapping," *Biophysical journal*, vol. 93, no. 4, pp. 1163-1174, 2007.

- [73] P. K. Huynh, A. Setty, H. Phan, and T. Q. Le, "Probabilistic domain-knowledge modeling of disorder pathogenesis for dynamics forecasting of acute onset," *Artificial intelligence in medicine*, vol. 115, p. 102056, 2021.
- [74] P. Huynh, L. Irish, O. P. Yadav, A. Setty, and T. T. Q. Le, "Causal Inference in Longitudinal Studies Using Causal Bayesian Network with Latent Variables," in *2022 Annual Reliability and Maintainability Symposium (RAMS)*, 2022: IEEE, pp. 1-7.
- [75] P. K. Huynh, A. R. Setty, Q. M. Tran, O. P. Yadav, N. Yodo, and T. Q. Le, "A domain-knowledge modeling of hospital-acquired infection risk in Healthcare personnel from retrospective observational data: A case study for COVID-19," *Plos one*, vol. 17, no. 11, p. e0272919, 2022.

Supplementary Information

Multifractality in Surface Potential for Cancer Diagnosis

Phat K. Huynh¹, Dang Nguyen², Grace Binder³, Sharad Ambardar², Trung Q. Le^{1,2}, and Dmitri V. Voronine^{2,4*}

¹ Department of Industrial and Management Systems Engineering, University of South Florida, Tampa, FL, 33620

² Department of Medical Engineering, University of South Florida, Tampa, FL, 33620

³ Department of Chemistry, University of South Florida, Tampa, FL, 33620

⁴ Department of Physics, University of South Florida, Tampa, FL, 33620

* Corresponding author: dmitri.voronine@gmail.com

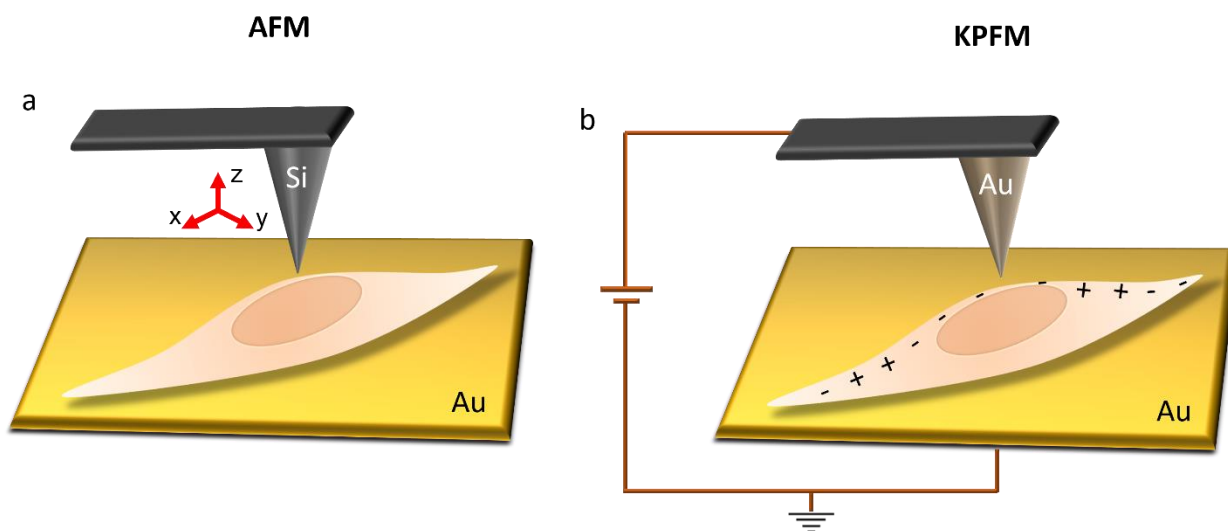


Figure S1. Schematic diagrams of the morphological AFM (a) and surface potential KPFM (b) imaging of cells.

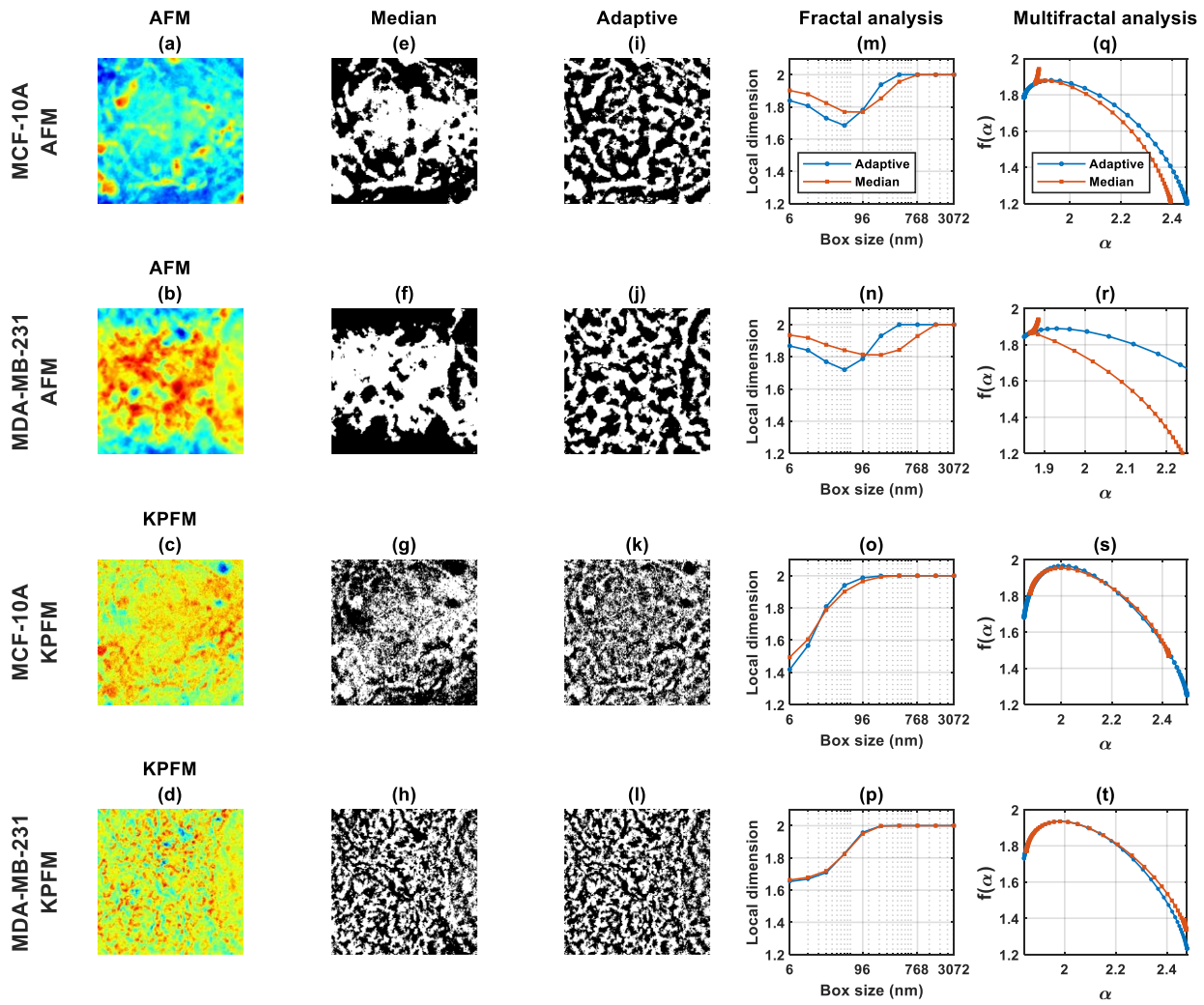


Figure S2. Typical representative examples of the AFM (a,b) and KPFM (c,d) images of the breast cell lines and their corresponding binarized images (e - l), local fractal dimensions (m - p), and multifractal spectra (q - t) using the adaptive and median value thresholding methods.

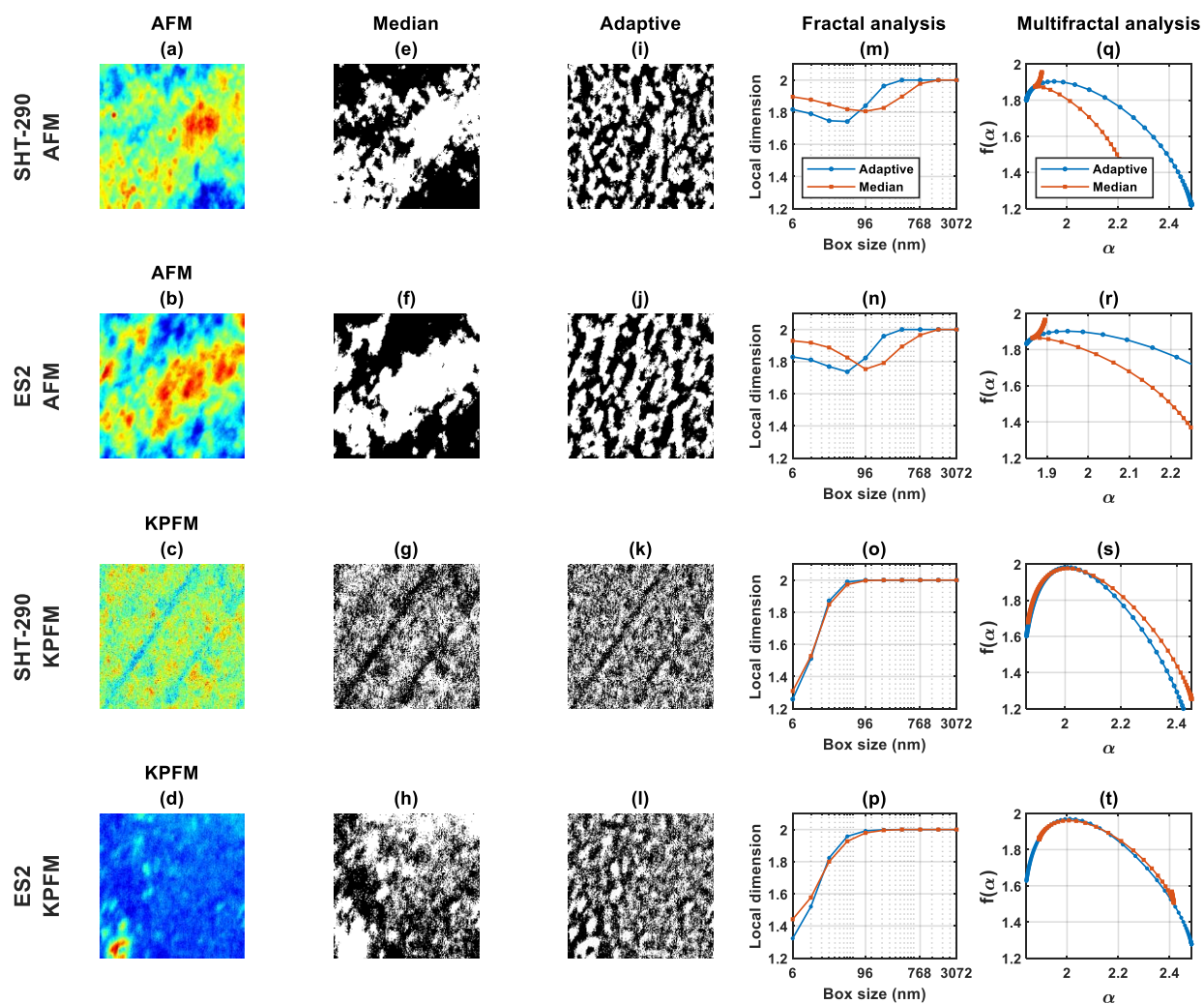


Figure S3. Typical representative examples of the AFM (a,b) and KPFM (c,d) images of the ovarian cell lines and their corresponding binarized images (e - l), local fractal dimensions (m - p), and multifractal spectra (q - t) using the adaptive and median value thresholding methods.

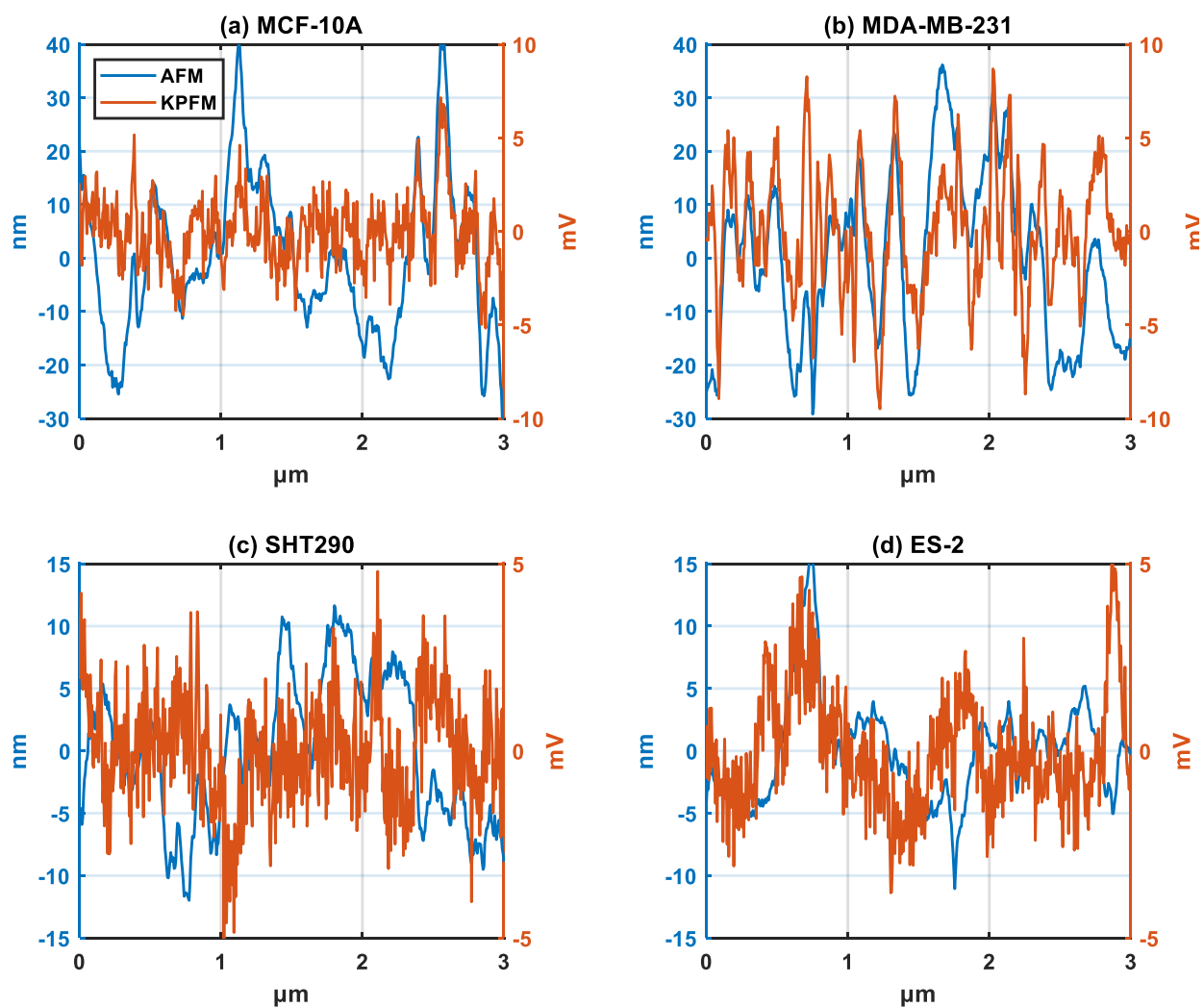


Figure S4. Typical representative AFM and KPFM profiles obtained from the $3 \times 3 \mu\text{m}^2$ scan areas used in the multifractal analysis.

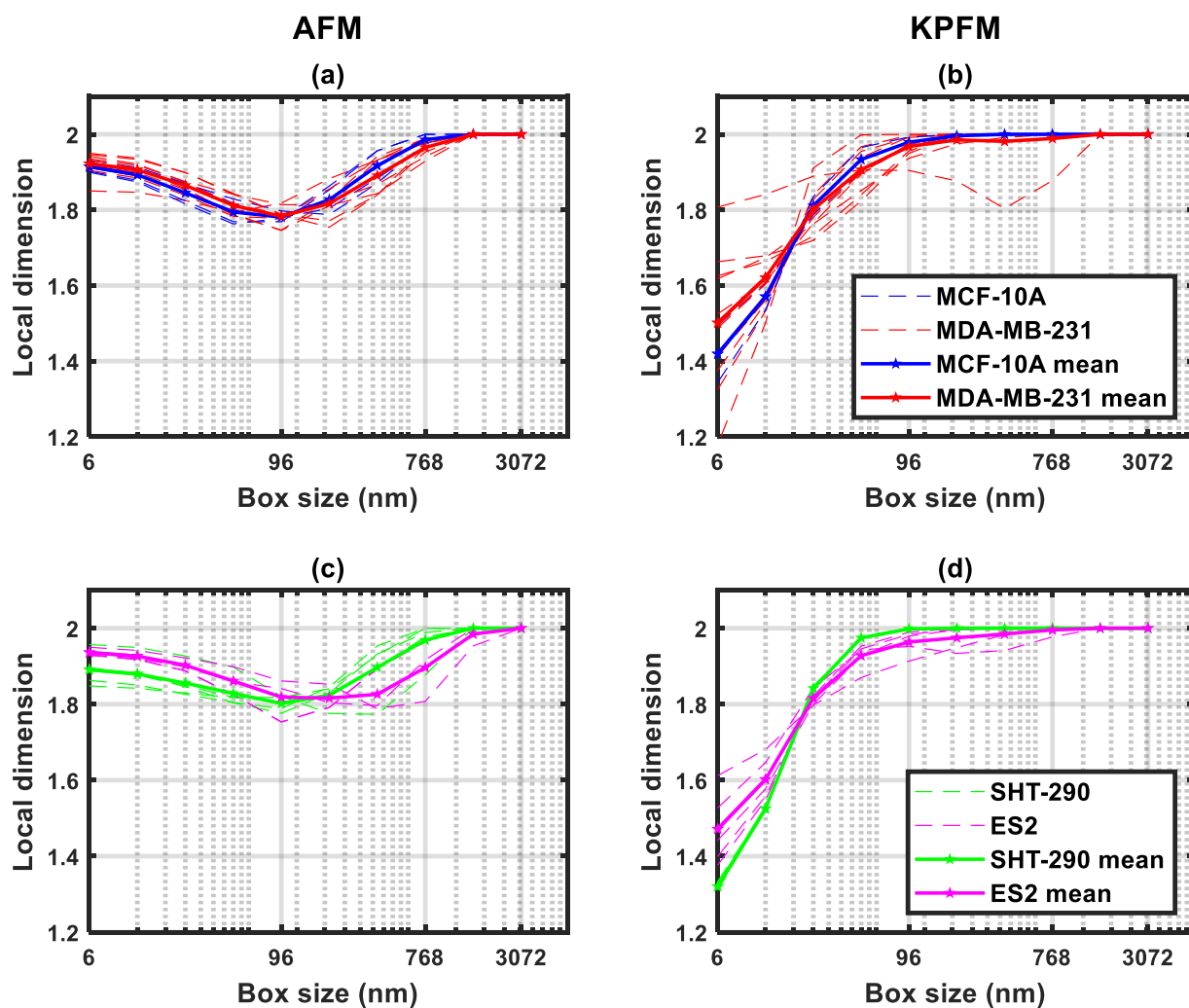


Figure S5. Fractal analysis of AFM and KPFM images using the box-counting method with median thresholding. Dependence of the local fractal dimension D_f as a function of the box size for individual cells (thin dashed lines) and mean data (thick solid lines).

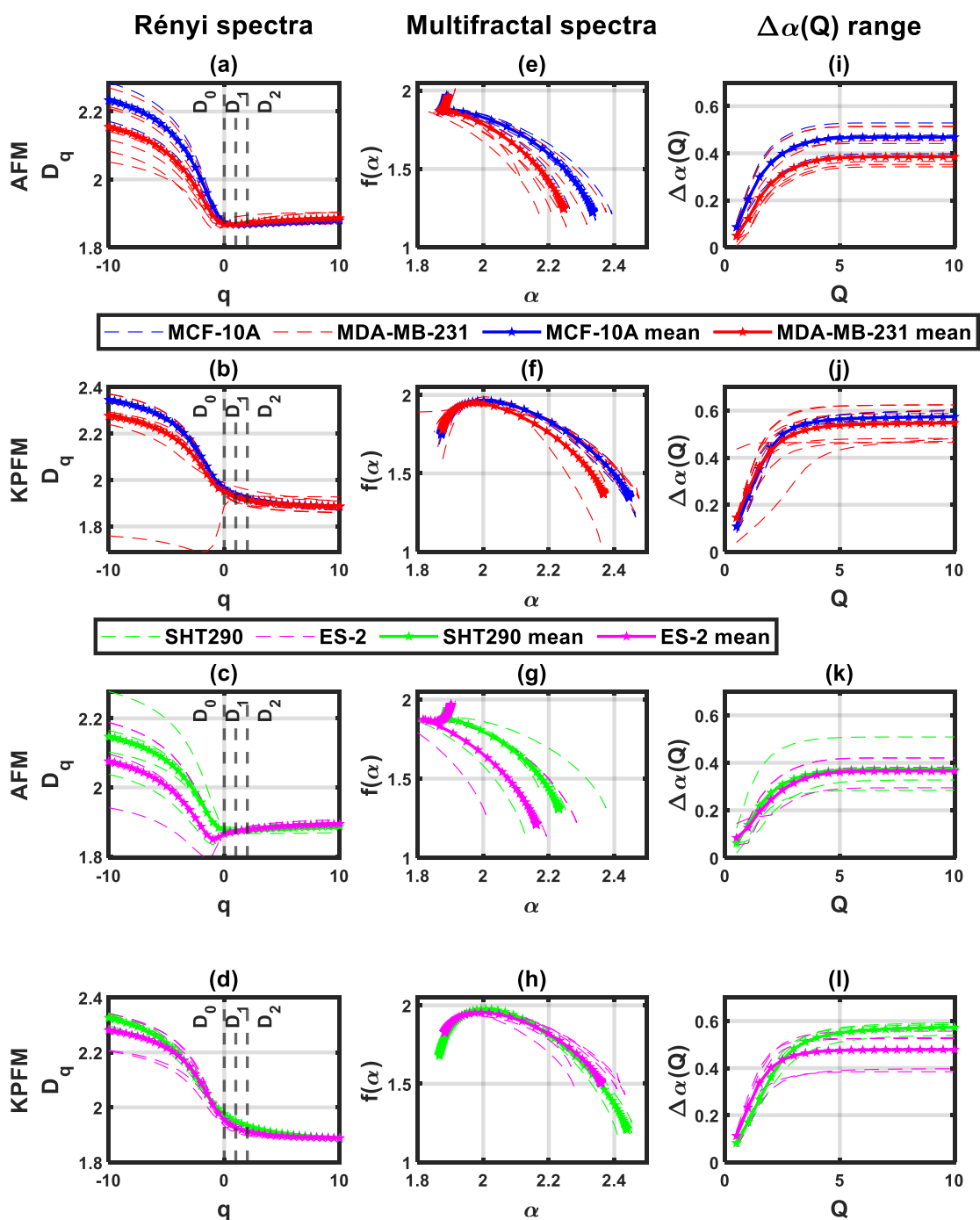


Figure S6. Rényi spectra (a – d), multifractal spectra (e - h), and singularity exponent range (i - l) obtained from multifractal analysis of median AFM and KPFM images of normal and cancer cells for individual areas (dashed lines) and averages (solid lines). Vertical dashed lines mark the D_0 , D_1 and D_2 values.

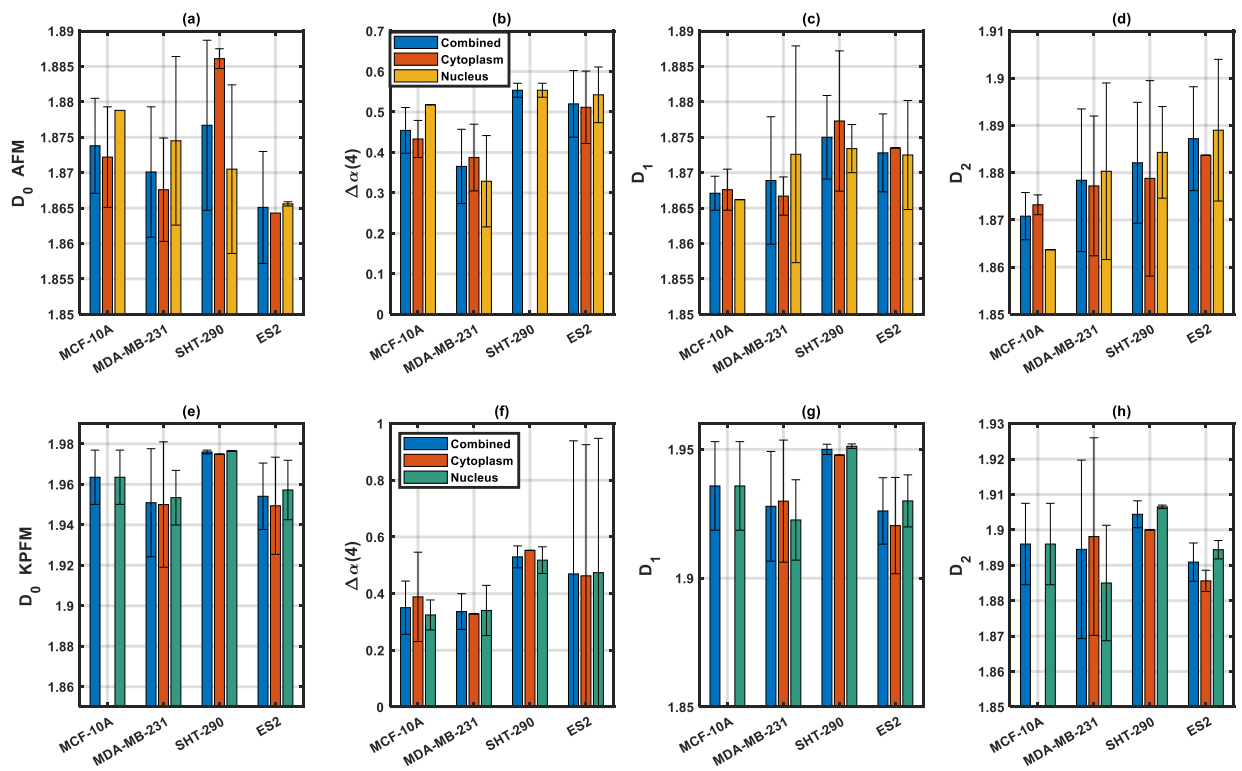


Figure S7. Comparison of the multifractal parameters D_0 , D_1 , D_2 , and $\Delta\alpha(4)$ from the combined and separate cytoplasm and nucleus regions using the median method.